Hypomorphic conditional deletion of E11/Podoplanin reveals a role in osteocyte dendrite elongation

Hypomorphic conditional deletion of E11/Podoplanin reveals a role in osteocyte dendrite elongation

Katherine A. Staines[1,2*]., Behzad Javaheri[3]., Peter Hohenstein[1]., Robert Fleming[1]., Ekele Ikpegbu[1,4]., Erin Unger[1]., Mark Hopkinson[3]., David J. Buttle[5]., Andrew A. Pitsillides[3]., Colin Farquharson[1]

[1] Roslin Institute and R(D)SVS, The University of Edinburgh, Easter Bush, Midlothian, UK [2] School of Applied Sciences, Edinburgh Napier University, Sighthill Campus, Edinburgh UK [3] Comparative Biomedical Sciences, Royal Veterinary College, Royal College Street, London, UK [4] Michael Okpara University of Agriculture, Nigeria [5] Dept of Infection, Immunity and Cardiovascular Disease, University of Sheffield, Sheffield UK

* Corresponding author

Katherine A. Staines

School of Applied Sciences, Edinburgh Napier University

Sighthill Campus, Edinburgh EH11 4BN

Email: k.staines@napier.ac.uk

Tel: 0131 455 3369

Running head: E11 is key in osteocyte dendrite elongation

Key words: Osteocytes; E11; osteocalcin; osteoblasts; dendrite

Total number of Figures: 5 Tables: 3

Contract grant sponsor: Arthritis Research UK & Biotechnology and Biological Sciences Research Council (BBSRC). **Contract grant number:** 20413 (ARUK) & BB/J004316/1 (BBSRC)

Abstract

The transmembrane glycoprotein E11/Podoplanin (Pdpn) has been implicated in the initial stages of osteocyte differentiation. However, its precise function and regulatory mechanisms are still unknown. Due to the known embryonic lethality induced by global *Pdpn* deletion, we have herein explored the effect of bone specific *Pdpn* knockdown on osteocyte form and function in the post-natal mouse. Extensive skeletal phenotyping of male and female 6-week-old *Oc*-cre;$Pdpn^{flox/flox}$ (cKO) mice and their $Pdpn^{flox/flox}$ controls (fl/fl) has revealed that *Pdpn* deletion significantly compromises tibial cortical bone microarchitecture in both sexes, albeit to different extents ($P<0.05$). Consistent with this, we observed an increase in stiffness in female cKO mice in comparison to fl/fl mice ($P<0.01$). Moreover, analysis of the osteocyte phenotype by phalloidin staining revealed a significant decrease in the dendrite volume ($P<0.001$) and length ($P<0.001$) in cKO mice in which deletion of *Pdpn* also modifies the bone anabolic loading response ($P<0.05$) in comparison to age-matched fl/fl mice. Together, these data confirm a regulatory role for *Pdpn* in osteocyte dendrite formation and as such, in the control of osteocyte function. As the osteocyte dendritic network is known to play vital roles in regulating bone modeling/remodelling, this highlights an essential role for *Pdpn* in bone homeostasis.

48 **Introduction**

49 Osteocytes are the most numerous of all the cells within bone and are critical
50 regulators of bone structure and function. Most original paradigms have proposed that
51 osteocytes are passive in their formation (Skerry et al., 1989; Nefussi et al., 1991;
52 Palumbo et al., 2004). Recent evidence, however, now indicates that initial
53 'embedding' involves their active contribution with vital transcriptional and dramatic
54 morphological transformations (Holmbeck et al., 2005). Osteocytes have a highly
55 specialized morphology with numerous dendritic processes extending from their cell
56 body, connecting them with other osteocytes and with cells lining the bone surfaces,
57 creating a large syncytium to enable cell-cell communications. Osteocytes play an
58 integral role in maintaining bone homeostasis by regulating bone modeling and
59 remodeling through their production of the Wnt inhibitor sclerostin, and through
60 communicating with bone-resorbing osteoclasts by RANKL production (Balemans et
61 al., 2001; Xiong et al., 2011; Nakashima et al., 2011; Dallas et al., 2013).

62 Although it is well recognized that osteocytes are derived from osteoblasts, the
63 mechanisms which govern this transition (osteocytogenesis) are yet to be fully
64 elucidated. Several different genes have been implicated in influencing
65 osteocytogenesis, one of which encodes for E11/Podoplanin (Pdpn) (Zhang et al.,
66 2006). Pdpn is a mucin-like, transmembrane glycoprotein, which undergoes O-
67 glycosylation leading to the production of different glycoforms. Pdpn is up-regulated
68 by hypoxia in the lung (Cao et al., 2003); IL-3 and PROX-1 in the lymphatic system
69 (Hong et al., 2002; Groger et al., 2004) and by TGF-β in fibrosarcoma cells (Suzuki et
70 al., 2005).

71 Few studies have investigated the precise function of Pdpn in osteocytes. We have
72 previously shown that Pdpn is expressed by early embedding osteocytes, thus

identifying it as a factor which likely contributes to the vital, early stages of osteocyte differentiation (Staines et al., 2016a). It is known that *Pdpn* expression in osteocytes is up-regulated in response to mechanical strain *in vivo* (Zhang et al., 2006) and that increased Pdpn expression, through overexpression in ROS 17/2.6 cells and through stabilization by proteasome inhibitors in MLO-A5 cells, leads to the formation of long dendritic processes (Sprague et al. 1996; Staines et al., 2016a). The formation of these cytoplasmic processes is abrogated in cells pre-treated with siRNA targeted against *Pdpn* (Zhang et al., 2006). Although these data support an important role for Pdpn in dendritic process formation, a key feature of the differentiating osteocyte, the underpinning mechanisms remain to be fully defined.

Whilst *in vitro* studies are informative, to fully disclose the biological function of Pdpn during *in vivo* osteocytogenesis and bone modeling/remodeling, it is essential to study an *in vivo* model of *Pdpn* deletion to enable a thorough examination of its functional role. Global deletion of *Pdpn* is perinatal lethal due to the essential role of Pdpn in lung and epithelial cell function (Zhang et al., 2006). We have therefore generated a *Pdpn* conditional knockout mouse to examine how deletion of *Pdpn* influences osteocytogenesis and the skeletal phenotype of these mice. We have used the well-characterized osteocalcin (OC)-cre promotor mouse (Zhang et al., 2002) as the expression of osteocalcin by late osteoblasts ensures that we eliminate Pdpn expression from late osteoblasts as they transition to the osteocyte phenotype. Using an osteocyte-specific cre mouse would have invalidated our experimental approach as it would have precluded our ability to study the role of Pdpn in osteocyte formation; osteoblasts would already have undergone differentiation into osteocytes. It is also pertinent to add that an osteocyte specific cre-promotor mouse does not currently exist. Here we show that a significant reduction in the expression of *Pdpn* in mice

affects tibial microarchitecture, compromises osteocyte dendrite elongation and thereby implicating Pdpn as a regulator of both osteocyte form and function.

Results

Oc-cre mediated bone-specific deletion of Pdpn

The genotypes from the breeding strategy were born at the expected Mendelian frequency, and all cKO mice exhibited survival indistinguishable from that of fl/fl control mice. To confirm that the *Pdpn* floxed allele was selectively deleted in bone in cKO mice, we performed PCR analysis using primers designed to specifically detect *Pdpn* alleles before (Tm1c) and after (Tm1d) cre-recombination. As expected, the Tm1d allele was only present in the cKO mice revealing selective deletion of *Pdpn* in bone (Fig. 1B). The presence of reduced levels of the retained Tm1c allele in the bones from cKO mice indicates that complete *Pdpn* deletion was, however, not achieved (Fig. 1B). This bone-selective hypomorphic expression of *Pdpn* in cKO mice was confirmed by immunohistochemical and immunoblotting data. In both genotypes, immunolabelling for Pdpn showed extensive expression throughout all soft tissues including the lung, kidney and liver (Fig. 1C). Pdpn immunolabelling was also observed in the growth plate chondrocytes of all mice (Fig. 1C). Osteoblasts in both the fl/fl and the cKO mice also stained positively for Pdpn. In the trabecular and cortical bone of the fl/fl mice, osteocytes and their dendritic processes exhibited positive immunolabelling for Pdpn (Fig. 1D). However, in the cKO mice, approximately 70% of osteocytes did not label positively for Pdpn, thereby indicating a significant reduction in bone Pdpn in these cKO mice ($P<0.001$; Fig. 1D & E). Similarly, western blotting revealed little Pdpn expression in the bones from cKO compared to fl/fl mice (Fig. 1F). Together these data confirm the hypomorphic loss of *Pdpn* expression selectively from bone in our cKO mice.

123 *Bone-selective ablation of Pdpn has no effect on the gross skeletal phenotype*

124 Analysis of total body weight (g) of male or female 6-week old mice showed no
125 significant differences between genotypes (male fl/fl – 20.4 ± 0.5; male cKO – 19.1 ±
126 0.4; female fl/fl – 16.3 ± 0.6; female cKO – 16.2 ± 0.5; n>4/genotype/sex). Similarly,
127 no differences were observed in the tibia lengths (mm) in cKO and fl/fl mice (male
128 fl/fl – 16.2 ± 0.1; male cKO – 16.1 ± 0.2; female fl/fl – 15.6 ± 0.2; female cKO – 15.5
129 ± 0.1; n>4/genotype/sex). Whole mount skeletal staining of mice also revealed no
130 obvious gross differences in Alcian blue or Alizarin Red staining between cKO and
131 fl/fl mice (Fig. 1G & H). Gait parameters of freely moving mice using the CatWalk
132 gait analysis system were also unchanged (Suppl. Fig 1). Together these data suggest
133 that the bone-selective deletion of *Pdpn* has no effect on the gross skeletal phenotype
134 of mice.

135 *Pdpn deletion significantly alters tibial cortical bone microarchitecture*

136 Assessment of cortical bone mass by μCT (CSA/mean cortical thickness) revealed
137 that *Pdpn* deletion produces statistically significant alterations in tibial cortical mass
138 and shape, to differing extents, in both male and female cKO compared to fl/fl control
139 mice. Specifically, CSA is unaffected in female cKO mice but is significantly lower
140 in male cKO compared with male fl/fl mice at ~40-65% of tibial length ($P<0.05$; Fig.
141 2A). In addition, mean cross sectional thickness was significantly lower at several
142 regions in male cKO compared to male fl/fl mice ($P<0.05$), however, *Pdpn* deletion
143 resulted in an increase in mean cross sectional thickness at several regions along the
144 tibial length in female cKO compared with fl/fl control mice ($P<0.05$; Fig. 2B).
145 Together these data indicate that the conditional deletion of *Pdpn* produces a deficit in
146 the cortical tibial microarchitecture in both male and female mice, with a greater
147 effect observed in the male mice. Despite this, no significant differences were

148 observed in the trabecular bone volume/tissue volume (BV/TV), trabecular number
149 (Tb.N), trabecular thickness (Tb.th), trabecular separation (Tb.Sp), or trabecular
150 pattern factor (Tb.Pf) in male or female cKO mice in comparison to age-matched fl/fl
151 control mice (Table 1).

152 *Hypomorphic deletion of Pdpn results in gender-dependent effects on tibial structural*
153 *parameters*

154 To provide an estimate of tibial resistance to bending forces, we calculated second
155 moment of area around minor (I_{min}) and major axes (I_{max}) (Fig. 3A & B). This
156 showed a reduction in I_{min} along the tibia length in female cKO compared to female
157 fl/fl which was most pronounced in midshaft and distal tibia ($P<0.05$, Fig. 3A).
158 Statically significant reduction in I_{min} was also apparent in the tibia of male cKO
159 compared with their male fl/fl controls, less so at the midshaft but more proximally
160 ($P<0.05$, Fig. 3A). Overall, the trend in cKO mice was for smooth lowering of I_{min}
161 proximodistally, which contrasts markedly from fluctuations in I_{min} along the tibia
162 length of age-matched fl/fl control mice. For I_{max}, the trend was similar for female
163 cKO and their fl/fl controls ($P<0.05$, Fig. 3B), however, the effect in male cKO
164 seemed to be more proximal and midshaft ($P<0.05$, Fig. 3B). Tibial ellipticity and
165 resistance to torsion (J) was mostly affected in female cKO compared with female
166 fl/fl ($P<0.05$, Fig. 3C & D) with only small regions affected in male cKO compared
167 with their male controls ($P<0.05$, Fig. 3C & D). This suggests that tibiae in female
168 cKO are weaker than in fl/fl control mice. Indeed our 3-point bending data shows a
169 52% increase in stiffness in the female cKO in comparison to fl/fl mice ($P<0.01$;
170 Table 2). No other significant differences were observed in bone strength, work to
171 rupture or maximum load between genotypes in either gender (Table 2).

172 *Bone selective Pdpn hypomorphism does not affect osteocyte differentiation but*
173 *causes disruption of the osteocyte dendritic network*

174 To examine how Pdpn deletion affects osteocytogenesis, we examined the
175 mineralization and differentiation potential of cultured primary calvaria osteoblasts
176 from Pdpn cKO and fl/fl mice. Alizarin red staining (Fig. 4A) and subsequent
177 quantification (Fig. 4B) revealed no significant differences in the mineralization
178 capabaility of Pdpn cKO primary osteoblasts in comparison to fl/fl mice. Consistent
179 with this, we observed no significant differences in the gene expression of the
180 osteocyte markers *Sost* and *Phex* in our Pdpn cKO cells at days 0, 7, 14 and 21 of
181 culture (Fig. 4C & D). Similarly, no significant differences in *Dmp1* expression were
182 observed at days 0, 7 and 14 although at day 21 of culture, there was a small
183 significant decrease in the expression of *Dmp1* in our Pdpn cKO cultures ($P<0.05$; Fig.
184 4E). Taken together, these data suggest that the bone selective hypomorphic deletion
185 of Pdpn does not influence osteocyte differentiation.

186 Due to the proposed role for Pdpn in osteocyte dendrite formation and elongation, we
187 sought to determine whether *Pdpn* deletion modifies osteocyte organisation by
188 measuring 3D morphometric parameters in high resolution images obtained from
189 nano-CT at the tibia–fibula junction. Our morphometric evaluation of the cortical
190 bone microarchitecture at the tibia–fibula junction shows that *Pdpn* deletion does not
191 affect numbers of osteocyte lacunae (N.Lc/Ct.TV; Table 3) or lacunar volume
192 (Lc.V/Ct.TV; Table 3). Interestingly, no significant effect on vascular porosity; canal
193 number (N.Ca; Table 3), density (N.Ca/Ct.TV; Table 3) and volume (normalised by
194 cortical tissue volume; Ca.V/Ct.TV; Table 3) was also evident in cKO bones.

195 Due to the reported function of the osteocyte in regulating bone remodeling and
196 phosphate homeostasis, we next sought to examine whether our cKO mice exhibit

197 differential expression of the osteocyte factor sclerostin, as well as serum phosphate.
198 We observed no apparent differences in the expression of sclerostin in our cKO mice
199 in comparison to fl/fl mice (Fig. 4F). Similarly, our assessment of osteoclast and
200 osteoblast numbers by TRAP and H&E staining, respectively and found no significant
201 differences in their number between cKO and fl/fl mice (Fig. 4G & H). Serum
202 phosphate levels were also similar in cKO and fl/fl mice (Fig. 4I). The osteocyte and
203 its canalicular-lacunar organisation also have another pivotal role in the bone's
204 adaptive response to mechanical stimuli. We therefore next sought to examine
205 whether tibiae deficient in *Pdpn* exhibit a modified response to mechanical loading.
206 As expected, and in line with previous data, fl/fl mice show a significant load-induced
207 increase in cortical bone cross-sectional thickness at the proximal diaphysis region of
208 the tibia ($P<0.01$, Fig. 5A - C). Although the scale of the load-induced increase was
209 statistically smaller than in fl/fl mice ($P<0.05$), cKO mice also exhibited a significant
210 increase in the tibial cross-sectional thickness in response to loading ($P<0.05$, Fig. 5A
211 - C; compared to contralateral control). As expected, in both our fl/fl and cKO mice, a
212 decrease in sclerostin immunolabelling was observed in cortical bone osteocytes of
213 the loaded limb in comparison to osteocytes of the unloaded contralateral limb (Fig.
214 5D). There were however no differences in osteocyte sclersotin expression between
215 loaded bones from fl/fl and cKO mice (Fig. 5D).

216 In the light of the relatively normal osteocyte organisation in cKO mice as disclosed
217 by nano-CT (Table 3), the difference in response of cKO and fl/fl control mice to
218 mechanical loading was somewhat surprising. Therefore, to determine whether this
219 deficit in load-related bone adaptation was associated with any specific change in
220 osteocyte morphology we next performed phalloidin staining of F-actin in fl/fl and
221 cKO cortical bone. Subsequent 3D rendering (Fig. 5E) and quantitative analysis of

222 osteocytes in the diaphyseal cortical bone confirmed our nano-CT data and revealed
223 no significant differences in the total number of osteocyte cell bodies (Fig. 5F), the
224 osteocytes cell body volume (Fig. 5G) or the osteocyte cell body sphericity (Fig. 5H)
225 in cKO bone in comparison to age-matched fl/fl bone. Similarly, no significant
226 differences were observed in the number of dendrites formed (Fig. 5I). However, a
227 significant decrease in the mean dendrite volume (Fig. 5J, $P<0.001$) and the dendrite
228 lengths (Fig. 5K, $P<0.001$) was noted in cKO in comparison to fl/fl mice, suggestive
229 of a role for Pdpn in attainment of fully developed dendrites.

230 **Discussion**

231 We, and others, have previously shown that Pdpn promotes osteocytogenesis and
232 dendrite formation *in vitro* (Zhang et al., 2006; Staines et al., 2016a). Our studies,
233 described herein, have for the first time successfully generated a bone-specific
234 conditional Pdpn hypomorphic mouse and we have confirmed a role for Pdpn in the
235 attainment of fully elongated osteocyte dendrites.

236 Previous attempts to decipher the *in vivo* role of Pdpn in osteocytogenesis have
237 involved global deletion of *Pdpn* in mice. In the lung, Pdpn is known as T1alpha or
238 RT140 and it is expressed on the apical surface of the lung epithelial cells (Dobbs et
239 al., 1988; Rishi et al., 1995). In mice, global deletion of this gene results in death at
240 birth due to respiratory failure. This is associated with the failure of type II alveolar
241 lung cells to differentiate into type I cells and as such, the lungs of these mice are
242 unable to inflate as normal (Ramirez et al., 2003). T1alpha deletion in mice also
243 produces lymphatic defects with pronounced lymphedema resulting in swelling of the
244 limbs at birth (Schacht et al., 2003). A previous comprehensive study has attempted to
245 analyze the effect of *Pdpn* deletion on the skeleton by generating a global *Pdpn*
246 knock-out mouse by targeting exon 1 (Zhang et al., 2006). Whilst these mice did not

express Pdpn in bone, the animals died soon after birth from suspected lung defect. Although the authors were unable to study the effects of *Pdpn* deletion on the postnatal skeleton they were able to make some important observations. The general appearance of the embryonic *Pdpn* null and wild-type mice was similar. More specifically, they found no significant differences in the length or diameter of the femur, or in the femur cortical thickness. They did report an increase in the body weight of the *Pdpn* null mice, however this was attributed to lymphedema resulting from limb swelling (Zhang et al., 2006).

By using the cre-LoxP system targeted to exon 3 of the *Pdpn* gene, we have generated bone specific conditional knockdown mice which exhibited survival indistinguishable from that of fl/fl control mice. This has for the first time allowed us to study the role of Pdpn in bone development in the post-natal mouse. The normal survival rates of cKO mice contrasts with perinatal lethality of global $Pdpn^{-/-}$ mice (Zhang et al., 2006). Here we used the well characterized osteocalcin-driven cre promotor to drive *Pdpn* deletion. *Oc*-cre expression has previously been reported to be exclusive to late osteoblasts, with onset of expression just before birth and continuing throughout the mature osteoblast lineage (Zhang et al., 2002). This has therefore allowed us to examine the structure and function of the postnatal skeleton in the presence of reduced Pdpn expression in bone, where we observed significant differences in tibial cortical bone microarchitecture and in the volume and length of osteocyte dendrites likely leading to downstream effects on the tibia's anabolic response to loading.

Osteocytes play a vital role in regulating bone remodeling and their vast dendritic network is critical to cell-cell communication, maintaining cell viability and allowing the transfer of nutrients and waste products (Dallas et al., 2013). Accumulating evidence has suggested that Pdpn may play a critical role in dendrite formation; in

MLO-Y4 cells, the deletion of *Pdpn* with siRNAs abrogated dendrite formation (Zhang et al., 2006). Conversely, the ectopic overexpression of *Pdpn* in keratinocytes induces plasma membrane extensions (Scholl et al., 1999), and in endothelial cells, the reorganisation of the actin cytoskeleton and the formation of long tube like structures (Schacht et al., 2003). Similarly, we have previously shown that stabilisation of Pdpn protein, through inhibition of endogenous proteasome activity, promotes dendrite formation through the RhoA/ROCK/ERM pathway (Staines et al., 2016a). RhoA is a small GTPase and a master regulator of various cellular processes such as cytokinetics, cytoskeletal regulation, and cell migration (Takai et al., 2001). Pdpn is able to co-localise with the ezrin, radixin and moesin (ERM) family of proteins which are essential for the linkage of the actin cytoskeleton to the plasma membrane (Scholl et al., 1999; Martin-Villar et al., 2006; Martin-Villar et al., 2014). Our present data suggests that Pdpn deletion does not affect osteocyte differentiation and instead, strongly support a role for Pdpn in the formation of full length dendritic processes. Despite this, we did not observe any differences in the expression of factors involved in the osteocytic regulation of bone remodeling and phosphate homeostasis. Normal sclerostin expression in osteocytes within bone of Pdpn cKO mice is consistent with a lack of change in osteocyte number, shape and size in these mice. It is possible that the hypomorphic deletion of Pdpn expression in osteocytes does not affect the osteocyte's ability to regulate bone remodeling. Rather, the decreased magnitude of bone accrual in response to mechanical loading is likely a consequence of inadequate dendrite formation and a lack of critical osteocyte mechanoregulatory function.

Mechanosensation and mechanotransduction were the earliest functions ascribed to the osteocyte and since then, there has been a wealth of evidence defining their role

297 and in particular, the role of the dendritic network in sensing mechanical loads. In
298 recent years, the complex biochemical pathways through which the osteocyte converts
299 its mechanical strain signals into a biological output have been unravelled. These
300 include intracellular calcium, nitric oxide, ATP and prostaglandins and these have
301 direct effects on osteoblasts to alter the bone microarchitecture (Dallas et al., 2013).
302 On this basis, we therefore speculate that the restricted osteocytic dendrite network
303 observed in our hypomorphic Pdpn cKO mice would likely lead to altered bone
304 geometry and microarchitecture; the reduced dendritic network impairs the ability of
305 the osteocyte to sense load and convert this to a biological signal affecting osteoblast
306 function. It would obviously therefore be of interest to examine the expression of the
307 aforementioned biochemical pathways in our Pdpn cKO mice in response to loading.
308 Moreover, as the bone mechanical properties, including stiffness, depend upon the
309 geometry of the bone shaft, it is likely that the reduction of the osteocyte dendritic
310 network affects the mechanical properties as a secondary effect through these changes
311 in the microarchitecture (Saffar et al., 2009).

312 Here we used whole bone μCT analysis to fully define these changes in
313 microarchitecture and determine the estimated strength and rigidity of the bone
314 through the study of the bone's cross sectional geometry. CSA is directly related to a
315 bone's strength against compressive forces applied equally throughout the bone;
316 factors such as bone shape and the effects of muscle contraction however result in
317 long bones experiencing bending and torsional forces (Javaheri et al., 2015). We
318 measured indices of rigidity, including maximum and minimum resistance against
319 bending forces in the cross section, second moment of area around minor axis (I_{min})
320 and second moment of area around major axis (I_{max}) in male and female cKO tibia and
321 their age-matched control mouse tibia. Our data, using this approach, revealed sex-

dependent differences in cortical bone microarchitecture and in our estimation of tibial resistance to bending forces in cKO mice in comparison to control mice. These differences suggest that bone responses to dysfunctional osteocyte form and function may be sex-dependent. Similarly the differences in the regional responses in both male and female bones suggests that *Pdpn* may play differential roles in bone development and function. Interestingly, Bonewald and colleagues found osteocyte Pdpn expression was increased in an ulna loading model, but that this increase was not consistent along the length of the diaphysis (Zhang et al., 2006). This regional requirement for *Pdpn* function during physiological loading in the post-natal mouse may explain the differences noted in structural parameters of the *Pdpn* cKO mouse and in the relatively minor, albeit significant, reductions in load-related increases in cortical thickness in the bones of these mice.

Despite these changes in bone microarchitecture and osteocyte form in our *Pdpn* cKO mice our data reveals no effect of *Pdpn* deletion on the gross phenotype. This suggests that whilst *Pdpn* plays a role in dendrite length and bone microarchitecture, there may be redundancy associated with the function of *Pdpn.* Possible candidates include Dentin matrix protein 1 (DMP1). DMP1 is an acidic phosphorylated extracellular matrix protein that is part of the Small; Integrin-Binding LIgand, N-linked Glycoprotein (SIBLING) family along with bone sialoprotein (BSP), osteopontin (OPN), dentin sialophosphoprotein (DSPP) and matrix extracellular phosphoglycoprotein (MEPE). All of these family members contain an RGD sequence for integrin binding and can bind to hydroxyapatite (Staines et al., 2012). DMP1 is highly expressed by osteocytes and is restricted to the dendritic processes. Deletion of DMP1 in mice causes remarkable defects in both tooth and bone (Ye et al., 2004; Ye et al., 2005). DMP1 knockout mice also display an abnormal lacuna-

canalicular system, with a reduction in the number of canaliculi and a 2-fold expanded osteocyte lacunae with rough, not smooth, lacunar walls (Lu et al., 2011). The authors of this elegant study also showed that this phenotype can be rescued by the re-expression of the 57-kDa C-terminal fragment of DMP1 (Lu et al., 2011). DMP1 has been demonstrated to bind to the hyaluronan receptor CD44, a membrane bound protein thought to interact with the ERM family of proteins that are involved in actin cytoskeleton rearrangement and as such, the formation of the osteocyte dendritic processes (Jain et al., 2002).

As we did not achieve complete cre-recombination and consequently not a complete knock-out of *Pdpn* expression (~70% reduction) it is also possible that a low level of *Pdpn* expression is sufficient to drive osteocytogenesis. A more complete knock-out of *Pdpn* expression may be required to reduce dendrite formation to a level where bone function is pathologically compromised. Our decision to use the osteocalcin-cre promotor mouse to drive deletion of Pdpn selectively in bone was based on the onset of OCN expression. Despite this, there have been previous reports of incomplete recombination when using these mice (Xiao et al., 2010). As such it might be prudent to attempt another cre driver mouse. Such examples would include the col 2.3 kb (Col 2.3-Cre) and 3.6 kb (Col 3.6-Cre) fragments of the rat Col1a1 promoter or the osterix-cre mouse (Liu et al., 2004; Rodda et al., 2006).

In summary, our data confirm a role for *Pdpn* in the formation of full length dendritic processes during osteocytogenesis and suggest that dysfunctional osteocyte dendrite formation is sufficient to alter the bone microarchitecture. The generation of a viable post-natal bone specific *Pdpn* cKO will enable future research into understanding the importance of *Pdpn* in osteocyte function, and in particular to the *in vivo* effects of dysfunctional osteocyte formation on bone homeostasis.

372 **Materials and methods**

373 *Generation of a Pdpn conditional knockout mouse*

374 We obtained floxed *Pdpn* mice from the EUCOMM/KOMP, MRC Harwell,
375 Oxfordshire UK and OC-cre mice as a kind gift from Thomas Clemens at John
376 Hopkins Medicine, Baltimore, USA (Zhang et al., 2002). *Pdpn* floxed mice were
377 designed with the *loxP* sites around exon 3 (Fig. 1A). Mice were crossed to generate
378 Oc-Cre;$Pdpn^{flox/flox}$ conditional knockout mice (cKO) as well as appropriate
379 $Pdpn^{flox/flox}$ control mice (fl/fl). PCR based genotyping was performed on mouse DNA
380 using a duplex PCR reaction for *Cre* (F: GCA TTA CCG GTC GAT GCA ACG AGT
381 GAT GAG; R: GAG TGA ACG AAC CTG GTC GAA ATC AGT GCG) and
382 *Fabpi200* (F: TGG ACA GGA CTG GAC CTC TGC TTT CCT AGA; R: TAG AGC
383 TTT GCC ACA TCA CAG GTC ATT CAG) and for *Pdpn* (F: TCC CAC ACC AGG
384 TTT TGT GT; R: CAG TGA GCC ATC TCT CCA GC). Mice were kept in
385 polypropylene cages, with light/dark 12-h cycles, at 21 ± 2°C, and fed *ad libitum* with
386 maintenance diet (Special Diet Services, Witham, UK). All experimental protocols
387 were approved by Roslin Institute's Animal Users Committee and the animals were
388 maintained in accordance with UK Home Office guidelines for the care and use of
389 laboratory animals. All analysis and data acquisition were completed on 6-week-old
390 mice and tissue obtained from them.

391 *Determination of Cre-mediated Recombination Efficiency*

392 To determine the specificity and efficiency of Cre-mediated recombination, PCR
393 analysis was performed on genomic DNA extracted from bones using a Qiagen DNA
394 extraction kit according to the manufacturer's instructions. Primers were specific for
395 alleles before recombination (Tm1c; F: TGG AAT GGC TGT GAG TTC TG; R:

CTA AAA TGG AGT TGG AGA TGG ATA C) and after recombination (Tm1d; F: TGA GCG AGC AGA GGT CCT AA; R: GCG TCT GGC ACT CTC AGA AG).

Primary osteoblast isolation and culture

Primary calvarial osteoblasts were obtained from 3-day-old Pdpn cKO and fl/fl mice by sequential enzyme digestion of excised calvarial bones using a four-step process as has previously been described (Staines et al., 2013) [1 mg/ml collagenase type II in Hanks' balanced salt solution (HBSS) for 10 min; 1 mg/ml collagenase type II in HBSS for 30 min; 4 mM EDTA for 10 min; 1 mg/ml collagenase type II in HBSS for 30 min]. The first digest was discarded and the cells were re-suspended in growth medium consisting of a-MEM (Invitrogen, Paisley UK) supplemented with 10% (v/v) FCS (Invitrogen) and 1% gentamycin (Invitrogen). Osteoblasts were seeded at a density of 1×10^4 cells/cm^2 and cultured for up to 21 days with the addition of 2.5 mM β-glycerophosphate and 50 μg/ml ascorbic acid. At days 0, 7, 14 and 21, Cells were either processed for RNA extraction or fixed in 4% paraformaldehyde and stained with 2% alizarin red (pH 4.2) for 5 min at room temperature. Alizarin red-stained cultures were extracted with 10% cetylpyridinium chloride for 10 min and optical density was measured at 570nm.

Gait analysis

Gait parameters of freely moving male mice were measured using the CatWalk gait analysis system (Noldus Information Technology, The Netherlands) as described previously (Masocha et al., 2009; Hammers et al., 2001). Each mouse was placed individually in the CatWalk walkway and allowed to walk freely and traverse from one side to the other of the walkway glass plate. Mice were habituated every day for two weeks prior to the test run, in which the gait of all mice was recorded three times

and analysed using the CatWalk system. Analysis of the recording generated a wide range of parameters; those analysed are detailed in Supplementary Table 1.

In vivo loading

12-week old male mice were isoflurane-anaesthetised and the right tibia loaded as described previously using a well-established model for comparing architectural load-induced changes in tibiae in control and mutant mice in which the contralateral left tibia is used as control (De Souza et al., 2005). Briefly, axial compressive loads were applied by a servo-hydraulic materials testing machine (Bose, UK) via custom-made cups which hold knee and ankle joints flexed and the tibia vertically. The loading pattern consisted of a trapezoidal wave, with peak 11N loads for the cKO and 12N for the WT mice for 0.05 s, rise and fall times 0.025 s each and baseline hold time of 9.9 s at 2 N (calibrated for peak strain level by finite element analysis) (Pereira et al., 2015). Forty cycles were applied in each loading episode. 12-week old male cKO and WT mice (n>3/genotype) were loaded 3 times per week for 2 weeks and left and right tibia dissected 3 days after the final loading episode.

Whole mount staining

Male mice were euthanized by CO_2 and incubated for 24 hours in tap water. Carcasses were then scalded in hot tap water to enable removal of the skin, skinned and eviscerated, and then fixed in 95% ethanol for 3-5 days. The preparations were then incubated in 0.015% Alcian blue (pH 0.75) for 24 hours to stain sulphated glycosaminoglycans in the cartilage, rinsed twice in 95% ethanol and fixed in 95% ethanol for another 2 days. Mice were then cleared of the remaining muscle by a 6 hour incubation in 1% KOH (w/v) and the bone was stained with fresh 0.005% Alizarin Red for 3 hours. Mice were then further cleared in 2% KOH (w/v) for 48 hours followed by decreasing concentrations of 2% KOH (w/v) in glycerol for 24 h

445 each (80:20, 60:40, 40:60 and 20:80, respectively). The skeletal preparations were
446 stored in 20:80 2% KOH:glycerol at room temperature.

447 *Tissue processing for histological techniques*

448 Soft tissues (liver, spleen, lung, heart and kidney) and tibia/femurs were dissected
449 from freshly killed male and female mice and fixed in 4% paraformaldehyde (PFA)
450 for 24 hours at 4^{o}C. Tibiae were subsequently decalcified in 10%
451 ethylenediaminetetracetic acid (EDTA/PBS, pH 7.4 at 4^{o}C; Sigma Aldrich, Dorset,
452 UK) for 3-4 weeks with regular changes. Soft tissues and legs were dehydrated and
453 processed to paraffin wax using standard procedures. Sections (5μm) were cut and
454 used for histological and immunohistochemical analysis. To analyse osteoclast and
455 osteoblast numbers, sections were reacted for tartrate-resistant acid phosphatase
456 activity (TRAP) and stained by H&E respectively, as described previously
457 (Erlebacher et al., 1996). Osteoclasts were quantified per mm^2 of trabecular bone, and
458 osteoblasts per mm of bone surface, in an identical region at an equivalent distance
459 beneath the growth plate in all samples.

460 *Immunohistochemistry*

461 For immunohistochemical analysis, sections were dewaxed in xylene and rehydrated.
462 Sections were incubated at 37 °C for 30 min in 1mg/ml trypsin for antigen demasking.
463 Endogenous peroxidases were blocked by treatment with 3% H_2O_2 in methanol
464 (Sigma). Ppdn antibodies (Polyclonal raised in Goat IgG; R&D systems) were used at
465 a dilution of 1/100; and sclerostin antibodies (Polyclonal raised in Goat IgG; R&D
466 systems) at a dilution of 1:200 with appropriate IgG controls. The Vectastain ABC
467 universal kit (Vector Laboratories, Peterborough, UK) was used according to the
468 manufacturer's instructions. The sections were dehydrated, counterstained with
469 haematoxylin and mounted in DePeX.

Phalloidin staining

Femurs from male mice were decalcified as described above and then cryoprotected in 30% sucrose (w/v) at 4^{o}C for 48 hours. The femora were cut in the mediolateral plane in serial longitudinal 20µm thick-sections using a cryostat and thaw-mounted on gelatin-coated slides for processing. Slides were dried at room temperature for 45 minutes, washed in PBS twice for 5 min each, and incubated with 0.1% Triton-X 100 (Sigma Aldrich) for 30 minutes and then rinsed with PBS. Slides were then incubated with Alexa Fluor 488-conjugated phalloidin (1:20; Life Technologies, Grand Island, NY) for 1 hour. Bone sections were washed in PBS and mounted in VectaShield (Vector Laboratories). Preparations were allowed to dry at room temperature for 12 hours.

Analysis of phalloidin staining

Sections were imaged on a Zeiss LSM 710 Laser Scanning Confocal Microscope with 488nm laser excitation and detection settings from 493 to 634nm. Z-stacks were produced with optimal Nyquist overlap settings using a 63x/1.4na oil immersion lens. Voxel sizes were 0.1x0.1x1.00µm in x,y,z planes respectively. A comparable region of interest was analysed for osteocyte parameters in all samples located in the diaphyseal cortical bone. Image stacks were imported into Bitplane Imaris 8.2.0 software and algorithms were created with Imaris FilamentTracer to render and measure dendritic processes. Surface rendering was used for osteocyte cell body measurements.

Micro-computed tomography (µCT) scanning

Tibiae from male and female mice were dissected and frozen at -20^{o}C until required. Scans were performed with an 1172 X-Ray Microtomograph (Skyscan, Belgium) to

evaluate bone geometry. High-resolution scans with an isotropic voxel size of 5 µm were acquired (50 kV, 200µA, 0.5 mm aluminium filter, 0.6° rotation angle, 2 frame averaging, exposure time 1650). The projection images were reconstructed using NRecon software version 1.6.9.4 (Skyscan, Belgium) to produce tomograms that underwent processing during reconstruction to correct for beam-hardening and ring artefacts.

Morphometrical analysis

a. Trabecular bone

For the trabecular analysis, the base of the growth plate was used as a standard reference point. Trabecular bone was analysed in a 1mm region of the proximal tibia 250 µm from this reference point (towards the diaphysis). Data were analysed with CtAn software (Skyscan) as previously described (Staines et al., 2016b).

b. *Whole bone cortical µCT analysis*

Whole bone analysis was performed on datasets derived from whole CT scans using BoneJ (version 1.13.14) a plugin for ImageJ, as previously described (Javaheri et al., 2015). Following segmentation, alignment and removal of fibula from the dataset, a minimum bone threshold was selected using a histogram based method in ImageJ which utilises all pixels in a stack to construct a histogram and was further confirmed using ImageJ "threshold function". The grey level threshold ranged between 22000-22100 and was applied to all datasets to separate higher density bone from soft tissues and air. This threshold was used in "Slice Geometry" function within BoneJ to calculate bone cross sectional area (CSA), second moment of area around the minor axis (I_{min}), second moment of area around the major axis (I_{max}), mean cortical thickness determined by local thickness in two dimensions (Ct.Th), ellipticity and

518 resistance to torsion (J). The most proximal and distal (10%) portions of the tibial
519 length were excluded from analysis, as these regions include trabecular bone

520 *Nano-computed tomography analysis*

521 The samples were placed in Orthodontic Wax (Kerr, CA, USA) at 50 kV and 200 μA,
522 9800 ms exposure time with a 0.25 mm aluminium filter (99.999% purity,
523 Goodfellow, Huntington, UK), voxel size of 0.6 μm, 360° at a rotation step of 0.25°.
524 Two-frame averaging was used to improve the signal-to-noise ratio. We analysed 300
525 consecutive images from the tibia–fibula junction from each sample. Using the CtAn
526 software, osteocyte lacunar indices were calculated by measuring the 3D parameters
527 of each discreet object within the volume of interest after segmentation as described
528 previously (Javaheri et al., 2015). Shape analysis of the lacunae was conducted
529 utilizing 'Analyze Particles' function in BoneJ.

530 *Mechanical testing*

531 A Lloyd LRX5 materials testing machine (Lloyd Instruments, West Sussex, UK)
532 fitted with a 100N load cell was used to determine bone stiffness and point of failure
533 of tibiae. The span was fixed at 10 mm, and the cross-head was lowered at 1 mm/min.
534 Data were recorded after every 0.2 mm change in deflection. Each bone was tested to
535 failure, with failure points being identified as the point of maximum load from the
536 load–extension curve. The maximum stiffness was defined as the maximum gradient
537 of the rising portion of this curve (Huesa et al., 2011).

538 **RNA extraction and quantitative real-time PCR (RT-qPCR)**

539 Total RNA was extracted using the RNEasy mini kit (Qiagen) according to the
540 manufacturer's instructions. RNA samples were reverse-transcribed into cDNA using
541 Superscipt II reverse transcriptase (Invitrogen). RT-qPCR was carried out in a

Stratagene Mx3000P cycler with each reaction containing 50ng template DNA, 250nM forward and reverse primers (Primer Design, Southampton UK) (*Sost*: F – TGAGAACAACCAGACCATGAAC, R – TCAGGAAGCGGGTGTAGTG; *Dmp1*: F – ATACCACAATACTGAATCTGAAAGC, R – CACTATTTGCCTGTCCCTCTG; *Phex*: F – CTAACCACCCACTCCCACTT, R – CCAATAGACTCCAAACCTGAAGA; *Atp5b*: sequences not available) and PrecisionPlus Mastermix (Primer Design). The Ct values for the samples were normalised to that of *Gapdh* and the relative expression was calculated using the ΔΔCt method (Livak and Schmittgen, 2001). The amplification efficiencies of all the primers were between 90–100%.

Western blotting

Femurs from male mice had their epiphyses removed and were flushed to remove bone marrow, snap frozen and lysed in RIPA buffer (Sigma), containing protease inhibitors (Roche). Protein content was determined using the DC protein assay (Bio-Rad Laboratories). The lysates were run on 10% Bis–Tris gels. Following transfer, nitrocellulose films were blocked in 5% milk, and probed overnight at 4^{o}C with Pdpn primary antibody (R&D systems; 1:1000). The nitrocellulose was subsequently incubated with peroxidase labelled rabbit anti-goat antibodies (Dako) for a further 90min. ECL detection reagents were used to visualise bands on hyperfilm (GE Healthcare, Bucks, UK). Where necessary, the nitrocellulose was stripped using Restore Plus Stripping Buffer (GE Healthcare). Densitometry of western blotting was measured on three independent samples using Image J.

Serum phosphate analysis

565 Immediately before termination, blood was collected and incubated on ice for 30
566 minutes, before centrifugation at 15,000*g* for 10 minutes. The serum supernatant was
567 stored at -80°C until analysed for phosphate levels using a colorimetric Phosphate
568 Assay Kit (Abcam; 1:100) according to the manufacturer's instructions.

569 *Statistical analysis*

570 Data are expressed as the mean ± S.E.M of at least 3 replicates per experiment.
571 Results were analysed blinded. For cortical bone, graphs were developed using the R
572 programming language "R", version 3.1.3 (R Foundation for Statistical Computing,
573 Vienna, Austria; http://www.r-project.org). Normality and homogeneity of variance
574 of all the data were checked using the Shapiro-Wilk and the Bartlett's test in R 3.1.3
575 respectively. Two-sample Student's-test was used to compare means between female
576 cKO and fl/fl, and between male cKO and fl/fl. Kruskal-Wallis test was employed if
577 either the normality or the homogeneity of variance assumptions were violated ($p \geq$
578 0.05). $P<0.05$ was considered to be significant and noted as *; P values of <0.01 and
579 <0.001 were noted as '**' and '***' respectively.

580 **Acknowledgements**

581 We are grateful to the Arthritis Research UK for funding this research (20413 and
582 20581) and Elaine Seawright for her assistance with the experiments detailed. We are
583 also extremely thankful to the BRF staff at the Roslin Institute, especially Gordon
584 Melville. We are also grateful to the Biotechnology and Biological Sciences Research
585 Council (BBSRC) for Institute Strategic Programme Grant Funding BB/J004316/1

586 **Author Contributions**

587 KAS, BJ, DJB, AAP & CF conceived and designed experiments and wrote the
588 manuscript; PH conceived and designed experiments; MH, EI, EU & RF performed
589 experiments and analysed data. All authors read, discussed and edited the manuscript.

Competing financial interests

All authors have no conflicts of interest with regards to competing financial interests

References

Balemans, W, Ebeling M, Patel N, Van Hul E, Olson P, Dioszegi M, Lacza C, Wuyts W, Van Den Ende J, Willems P, Paes-Alves AF, Hill S, Bueno M, Ramos FJ, Tacconi P, Dikkers FG, Stratakis C, Lindpaintner K, Vickery B, Foernzler D, Van Hul W. 2001. Increased bone density in sclerosteosis is due to the deficiency of a novel secreted protein (SOST). *Human molecular genetics* **10**, 537-543.

Cao YX, Ramirez MI, & Williams, MC. 2003. Enhanced binding of Sp1/Sp3 transcription factors mediates the hyperoxia-induced increased expression of the lung type I cell gene T1alpha. *Journal of cellular biochemistry* **89**, 887-901.

Dallas SL., Prideaux M, & Bonewald LF. 2013. The osteocyte: an endocrine cell ... and more. *Endocrine reviews* **34**, 658-690

De Souza RL, Matsuura M, Eckstein F, Rawlinson SC, Lanyon LE, Pitsillides AA. 2005. Non-invasive axial loading of mouse tibiae increases cortical bone formation and modifies trabecular organization: a new model to study cortical and cancellous compartments in a single loaded element. *Bone* **37**, 810-818.

Dobbs LG, Williams MC, & Gonzalez R. 1988 Monoclonal antibodies specific to apical surfaces of rat alveolar type I cells bind to surfaces of cultured, but not freshly isolated, type II cells. *Biochimica et biophysica acta* **970**, 146-156.

Groger M, Loewe R, Holnthoner W, Embacher R, Pillinger M, Herron GS, Wolff K, Petzelbauer P. 2004. IL-3 induces expression of lymphatic markers Prox-1 and podoplanin in human endothelial cells. *Journal of immunology* **173**, 7161-7169.

Hamers FP, Lankhorst AJ, van Laar TJ, Veldhuis WB, Gispen WH. 2001. Automated quantitative gait analysis during overground locomotion in the rat: its application to spinal cord contusion and transection injuries. *Journal of neurotrauma* **18**, 187-201.

Holmbeck K, Bianco P, Pidoux I, Inoue S, Billinghurst RC, Wu W, Chrysovergis K, Yamada S, Birkedal-Hansen H, Poole AR. 2005. The metalloproteinase MT1-MMP is required for normal development and maintenance of osteocyte processes in bone. *Journal of cell science* **118**, 147-156.

Hong YK, Harvey N, Noh YH, Schacht V, Hirakawa S, Detmar M, Oliver G. 2002. Prox1 is a master control gene in the program specifying lymphatic endothelial cell fate. *Developmental dynamics : an official publication of the American Association of Anatomists* **225**, 351-357.

Huesa C, Yadav MC, Finnilä MA, Goodyear SR, Robins SP, Tanner KE, Aspden RM, Millán JL, Farquharson C. 2011. PHOSPHO1 is essential for mechanically competent mineralization and the avoidance of spontaneous fractures. *Bone* 4**8**, 1066-1074.

Jain A, Karadag A, Fohr B, Fisher LW, Fedarko NS. 2002. Three SIBLINGs (small integrin-binding ligand, N-linked glycoproteins) enhance factor H's cofactor activity enabling MCP-like cellular evasion of complement-mediated attack. *The Journal of biological chemistry* **277**, 13700-13708.

Javaheri, B., Carriero A, Staines KA, Chang YM, Houston DA, Oldknow KJ, Millan JL, Kazeruni BN, Salmon P, Shefelbine S, Farquharson C, Pitsillides AA. 2015.

Phospho1 deficiency transiently modifies bone architecture yet produces consistent modification in osteocyte differentiation and vascular porosity with ageing. *Bone* **81**, 277-291.

Liu F, Woitge HW, Braut A, Kronenberg MS, Lichtler AC, Mina M, Kream BE. 2004. Expression and activity of osteoblast-targeted Cre recombinase transgenes in murine skeletal tissues. *The International journal of developmental biology* **48**, 645-653.

Livak KJ, Schmittgen TD. 2001. Analysis of relative gene expression data using real-time quantitative PCR and the 2(-Delta Delta C(T)) method. *Methods* **25**:402–408.

Lu Y, Yuan B, Qin C, Cao Z, Xie Y, Dallas SL, McKee MD, Drezner MK, Bonewald LF, Feng JQ. 2011. The biological function of DMP-1 in osteocyte maturation is mediated by its 57-kDa C-terminal fragment. *J Bone Miner Res* **26**, 331-340.

Martín-Villar E, Megías D, Castel S, Yurrita MM, Vilaró S, Quintanilla M. 2006. Podoplanin binds ERM proteins to activate RhoA and promote epithelial-mesenchymal transition. *Journal of cell science* **119**, 4541-4553.

Martín-Villar E, Borda-d'Agua B, Carrasco-Ramirez P, Renart J, Parsons M, Quintanilla M, Jones GE. 2014. Podoplanin mediates ECM degradation by squamous carcinoma cells through control of invadopodia stability. *Oncogene* **34**, 4531-4544.

Masocha W, Parvathy SS. 2009. Assessment of weight bearing changes and pharmacological antinociception in mice with LPS-induced monoarthritis using the Catwalk gait analysis system. *Life Sci.* **85**, 462-469.

Nakashima T, Takayanagi H. 2011. New regulation mechanisms of osteoclast differentiation. *Annals of the New York Academy of Sciences* **1240**, E13-18.

Nefussi JR, Sautier JM, Nicolas V, Forest N. 1991. How osteoblasts become osteocytes: a decreasing matrix forming process. *Journal de biologie buccale* **19**, 75-82.

Palumbo C, Ferretti M, Marotti G. 2004. Osteocyte dendrogenesis in static and dynamic bone formation: an ultrastructural study. *The anatomical record. Part A, Discoveries in molecular, cellular, and evolutionary biology* **278**, 474-480.

Pereira AF, Javaheri B, Pitsillides AA, Shefelbine, SJ. 2015. Predicting cortical bone adaptation to axial loading in the mouse tibia. *Journal of the Royal Society, Interface / the Royal Society* **12**, 0590.

Ramirez MI, Millien G, Hinds A, Cao Y, Seldin DC, Williams MC. 2003. T1alpha, a lung type I cell differentiation gene, is required for normal lung cell proliferation and alveolus formation at birth. *Developmental biology* **256**, 61-72.

Rishi AK, Joyce-Brady M, Fisher J, Dobbs LG, Floros J, VanderSpek J, Brody JS, Williams MC. 1995. Cloning, characterization, and development expression of a rat lung alveolar type I cell gene in embryonic endodermal and neural derivatives. *Developmental biology* **167**, 294-306.

Rodda SJ, McMahon AP. 2006. Distinct roles for Hedgehog and canonical Wnt signaling in specification, differentiation and maintenance of osteoblast progenitors. *Development* **133**, 3231-3244.

Saffar KP, Jamilpour N, Rajaai SM. 2009. How does the bone shaft geometry affect its Bending Properties? *Am. J. Appl. Sci.* **6**(3): 463-470.

Schacht V, Ramirez MI, Hong YK, Hirakawa S, Feng D, Harvey N, Williams M, Dvorak AM, Dvorak HF, Oliver G, Detmar M. 2003. T1alpha/podoplanin deficiency

disrupts normal lymphatic vasculature formation and causes lymphedema. *EMBO J.* **22**, 3546-3556.

Scholl FG, Gamallo C, Vilaro S, Quintanilla M. 1999. Identification of PA2.26 antigen as a novel cell-surface mucin-type glycoprotein that induces plasma membrane extensions and increased motility in keratinocytes. *Journal of cell science* **112** (Pt 24), 4601-4613.

Skerry TM, Bitensky L, Chayen J, Lanyon LE. 1989. Early strain-related changes in enzyme activity in osteocytes following bone loading in vivo. *J Bone Miner Res* **4**, 783-788.

Sprague L, Wetterwald A, Heinzman U, Atkinson MJ. 1996. Phenotypic changes following over-expression of sense or antisense E11 cDNA in ROS 17/2.8 cells. *J Bone Miner Res* **11**, 151-151.

Staines KA, Macrae VE, Farquharson C. 2012. The importance of the SIBLING family of proteins on skeletal mineralisation and bone remodelling. *The Journal of endocrinology* **214**, 241-255.

Staines KA, Zhu D, Farquharson C, Macrae VE. 2013. Identification of novel regulators of osteoblast matrix mineralization by time series transcriptional profiling. *J Bone Mineral Metab*. **32**:240–251.

Staines KA, Prideaux M, Allen S, Buttle DJ, Pitsillides AA, Farquharson C. 2016a. E11/Podoplanin Protein Stabilization Through Inhibition of the Proteasome Promotes Osteocyte Differentiation in Murine in Vitro Models. *J. Cell. Physiol*. **231**, 1392-1404.

Staines KA, Madi K, Mirczuk SM, Parker S, Burleigh A, Poulet B, Hopkinson M, Bodey AJ, Fowkes RC, Farquharson C, Lee PD, Pitsillides AA. 2016b. Endochondral Growth Defect and Deployment of Transient Chondrocyte Behaviors Underlie Osteoarthritis Onset in a Natural Murine Model. *Arthritis & rheumatology* **68**, 880-891.

Suzuki H, Amizuka N, Oda K, Li M, Yoshie H, Ohshima H, Noda M, Maeda T. 2005. Histological evidence of the altered distribution of osteocytes and bone matrix synthesis in klotho-deficient mice. *Archives of histology and cytology* **68**, 371-381.

Takai Y, Sasaki T, Matozaki T. 2001. Small GTP-binding proteins. *Physiol. Rev.* **81**, 153-208.

Xiao Z, Zhang S, Cao L, Qiu N, David V, Quarles LD. 2010. Conditional disruption of Pkd1 in osteoblasts results in osteopenia due to direct impairment of bone formation. *The Journal of biological chemistry* **285**, 1177-1187.

Xiong J, Onal M, Jilka RL, Weinstein RS, Manolagas SC, O'Brien CA. 2011 Matrix-embedded cells control osteoclast formation. *Nat. Med.* **17,** 1235-1241.

Ye L, MacDougall M, Zhang S, Xie Y, Zhang J, Li Z, Lu Y, Mishina Y, Feng JQ. 2004. Deletion of dentin matrix protein-1 leads to a partial failure of maturation of predentin into dentin, hypomineralization, and expanded cavities of pulp and root canal during postnatal tooth development. *The Journal of biological chemistry* **279**, 19141-19148.

Ye L, Mishina Y, Chen D, Huang H, Dallas SL, Dallas MR, Sivakumar P, Kunieda T, Tsutsui TW, Boskey A, Bonewald LF, Feng JQ. 2005. Dmp1-deficient mice display severe defects in cartilage formation responsible for a chondrodysplasia-like phenotype. *The Journal of biological chemistry* **280**, 6197-6203.

727 Zhang M, Xuan S, Bouxsein ML, von Stechow D, Akeno N, Faugere MC, Malluche
728 H, Zhao G, Rosen CJ, Efstratiadis A, Clemens TL. 2002. Osteoblast-specific
729 knockout of the insulin-like growth factor (IGF) receptor gene reveals an essential
730 role of IGF signaling in bone matrix mineralization. *The Journal of biological*
731 *chemistry* **277**, 44005-44012.
732 Zhang K, Barragan-Adjemian C, Ye L, Kotha S, Dallas M, Lu Y, Zhao S, Harris M,
733 Harris SE, Feng JQ, Bonewald LF.2006. E11/gp38 selective expression in osteocytes:
734 regulation by mechanical strain and role in dendrite elongation. *Mol. Cell. Biol*. **26**,
735 4539-4552.
736

737 **Figure Legends**

738 **Figure 1. (A)** Schematic of the *Pdpn* floxed allele before and after deletion of the
739 loxP cassette containing exon 3 via osteocalcin cre (*Oc*-cre) mediated recombination.
740 **(B)** PCR analysis of genomic DNA from the long bones of fl/fl, and cKO mice with
741 primers for the Tm1c allele (before cre recombination), and the Tm1d allele (~440bp,
742 after cre recombination). **(C)** Immunohistochemical labelling of Pdpn in the lung,
743 kidney, spleen, heart, liver, muscle, and growth plate, of 6-week old mice. Images are
744 representative of n=4/sex/genotype. Scale bar = 20μm. **(D)** Immunohistochemical
745 labelling of Pdpn in the trabecular bone and cortical bone of 6-week old mice. Arrows
746 are pointing at embedded osteocytes within the trabecular and cortical bone and their
747 dendritic processes projecting from the cell bodies. Images are representative of
748 n=4/sex/genotype. Scale bar = 20μm. **(E)** Quantification of osteocytes positive for
749 Pdpn immunolabelling relative to negatively labelled osteocytes (n=3/genotype)
750 $P<0.001$*** **(F)** Western blotting for Pdpn (~37kDa) in cortical bone protein lysates
751 from 6-week old mice. β-actin was used as a loading control. Whole mount Alcian
752 Blue and Alizarin Red stained skeletal preparations of 6- week old male **(G)** fl/fl, and
753 **(H)** cKO mice (scale bar = 10mm) including hindlimb and calvaria preparations (scale
754 bar = 5mm).

Figure 2. Whole bone analyses of cortical bone between 10–90% of total tibial length, excluding proximal and distal metaphyseal bone, of female fl/fl (brown), female cKO (orange), male fl/fl (black) and male cKO (grey) tibia at 6 weeks of age showing **(A)** cross sectional area (CSA; mm^2) **(B)** mean cross sectional thickness (mm). Graphs represent mean ± S.E.M, n=4/group. $P<0.05$ was considered to be significant and P values of $p\leq0.01$-0.05 were noted as green, $p\leq0.001$-0.01 as yellow, and $p\leq0.000$-0.001 as red. Not significant is noted as blue.

Figure 3. Whole bone analyses of cortical bone between 10–90% of total tibial length, excluding proximal and distal metaphyseal bone, of female fl/fl (brown), female cKO (orange), male fl/fl (black) and male cKO (grey) tibia at 6 weeks of age showing **(A)** I_{min} (mm^4) **(B)** I_{max} (mm^4) **(C)** ellipticity **(D)** resistance to torsion **(**J; mm^4) Graphs represent mean ± S.E.M, n=4/group. $P<0.05$ was considered to be significant and P values of $p\leq0.01$-0.05 were noted as green, $p\leq0.001$-0.01 as yellow, and $p\leq0.000$-0.001 as red. Not significant is noted as blue.

Figure 4. (A) Alizarin red staining of primary osteoblast cultures from Pdpn cKO and fl/fl mice over a 21 day culture period. (B) Quantification of Alizarin red staining. RT-qPCR analysis of osteocyte marker genes **(C)** *Sost* **(D)** *Phex* **(E)** *Dmp1* in mineralizing primary osteoblast cultures from Pdpn cKO and fl/fl mice over a 21 day culture period. **(F)** Immunohistochemical labeling of sclerostin in the cortical bone of 6-week old mice. Arrows are pointing at embedded osteocytes within the cortical bone and their dendritic processes projecting from the cell bodies. Images are representative of n=4/sex/genotype. Scale bar = 20μm. **(G)** Osteoclast cell numbers ($OC.N/mm^2$) in the trabecular bone of 6-week old cKO and fl/fl mice (n=4/genotype) **(H)** Osteoblast cell numbers (OB.N/mm bone surface (BS)) in the trabecular bone of 6-week old cKO and fl/fl mice (n=4/genotype) **(I)** Serum phosphate levels in cKO and

780 fl/fl mice (n=6/genotype). Data are represented as mean ± S.E.M. P<0.05*, P<0.01**,
781 P<0.001***.

782 **Figure 5.** Representative images of fl/fl and cKO mice in **(A)** control **(B)** loaded
783 limbs. **(C)** Cortical cross-sectional thickness at 37% of the tibia length as assessed by
784 microCT analysis. **(D)** Immunohistochemical labeling of sclerostin in osteocytes of
785 cortical bone of loaded and control 6-week old Pdpn cKO and fl/fl mice. . Arrows are
786 pointing at embedded osteocytes within the cortical bone and their dendritic processes
787 projecting from the cell bodies. Images are representative of n=4/sex/genotype. Scale
788 bar = 20μm. **(E)** Laser confocal z-stack, single channel outlining phalloidin-Factin
789 staining was imaged in the cortical bone. Imaris cell surface rendering was applied to
790 cell bodies and Imaris FilamentTracer applied to dendritic processes and these were
791 coloured according to length. Quantification of osteocyte parameters in 6-week old
792 male fl/fl, and cKO **(F)** Total number of complete cell bodies in 3 volume fields. **(G)**
793 Cell body volume (μm^3) **(H)** Cell body sphericity **(I)** Total number of dendrites in 3
794 volume fields **(J)** Dendrite volume (μm^3) **(K)** Dendrite length (μm). Data are
795 represented as mean ± S.E.M. P<0.05*, P<0.01**, P<0.001***.

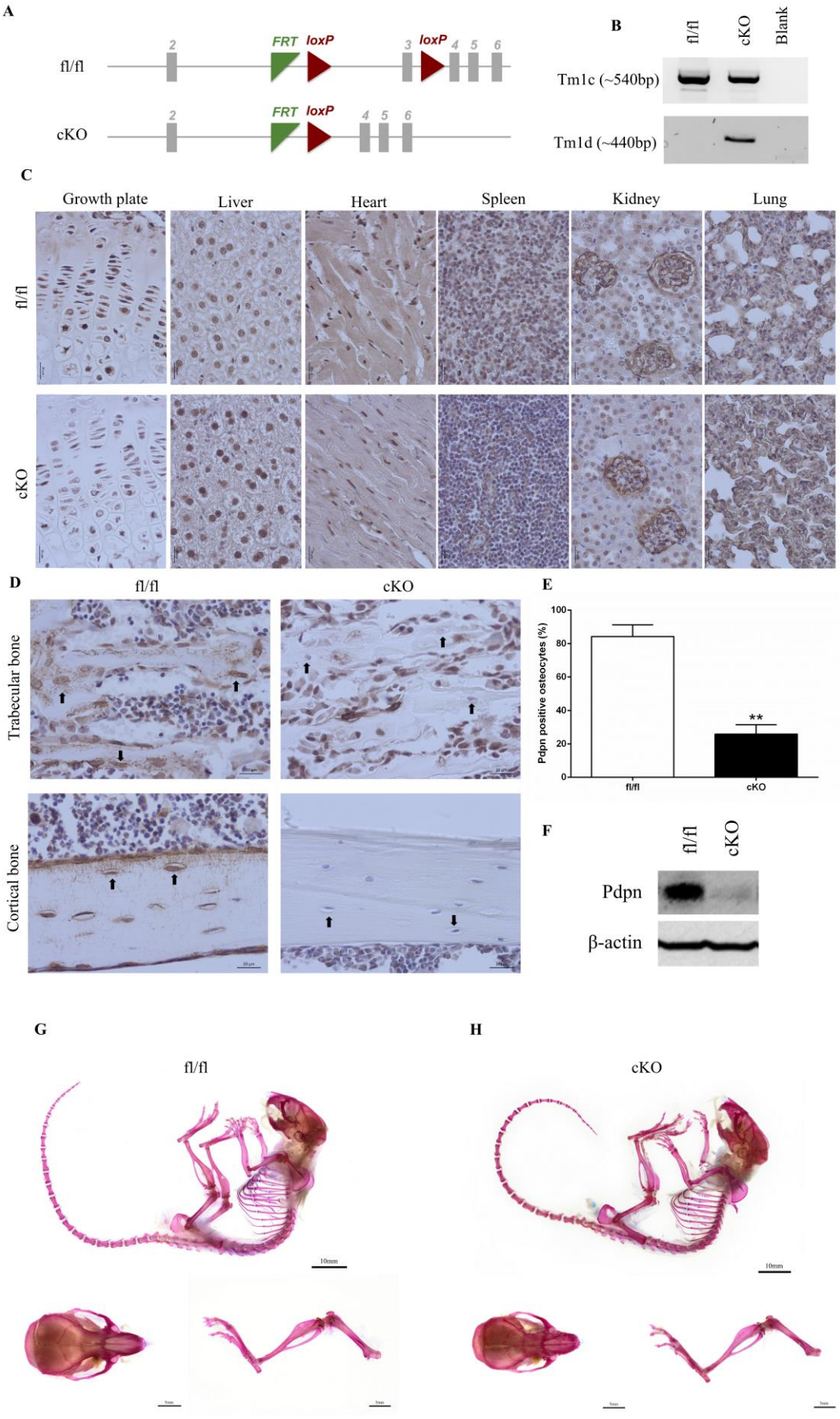
A
fl/fl
cKO
FRT
loxP
2
3
4
5
6
B
fl/fl
cKO
Blank
Tm1c (~540bp)
Tm1d (~440bp)
C
Growth plate
Liver
Heart
Spleen
Kidney
Lung
fl/fl
cKO
D
fl/fl
cKO
Trabecular bone
Cortical bone
E
Pdpn positive osteocytes (%)
100
80
60
40
20
0
**
fl/fl
cKO
F
fl/fl
cKO
Pdpn
β-actin
G
fl/fl
10mm
H
cKO
10mm

Figure 1

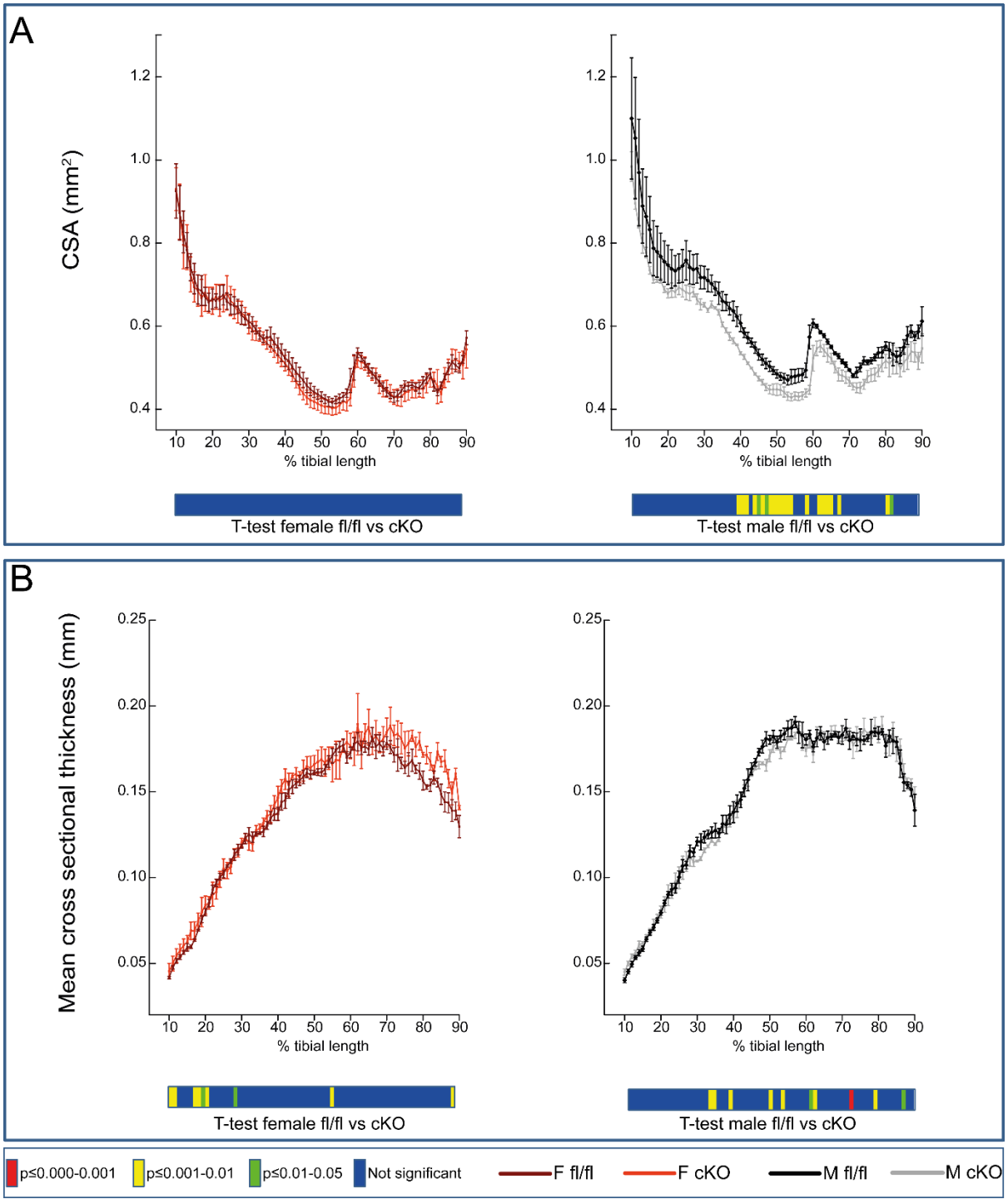
A
CSA (mm²)
1.2
1.0
0.8
0.6
0.4
10 20 30 40 50 60 70 80 90
% tibial length
T-test female fl/fl vs cKO
T-test male fl/fl vs cKO
B
Mean cross sectional thickness (mm)
0.25
0.20
0.15
0.10
0.05
10 20 30 40 50 60 70 80 90
% tibial length
T-test female fl/fl vs cKO
T-test male fl/fl vs cKO
p≤0.000-0.001
p≤0.001-0.01
p≤0.01-0.05
Not significant
F fl/fl
F cKO
M fl/fl
M cKO

Figure 2

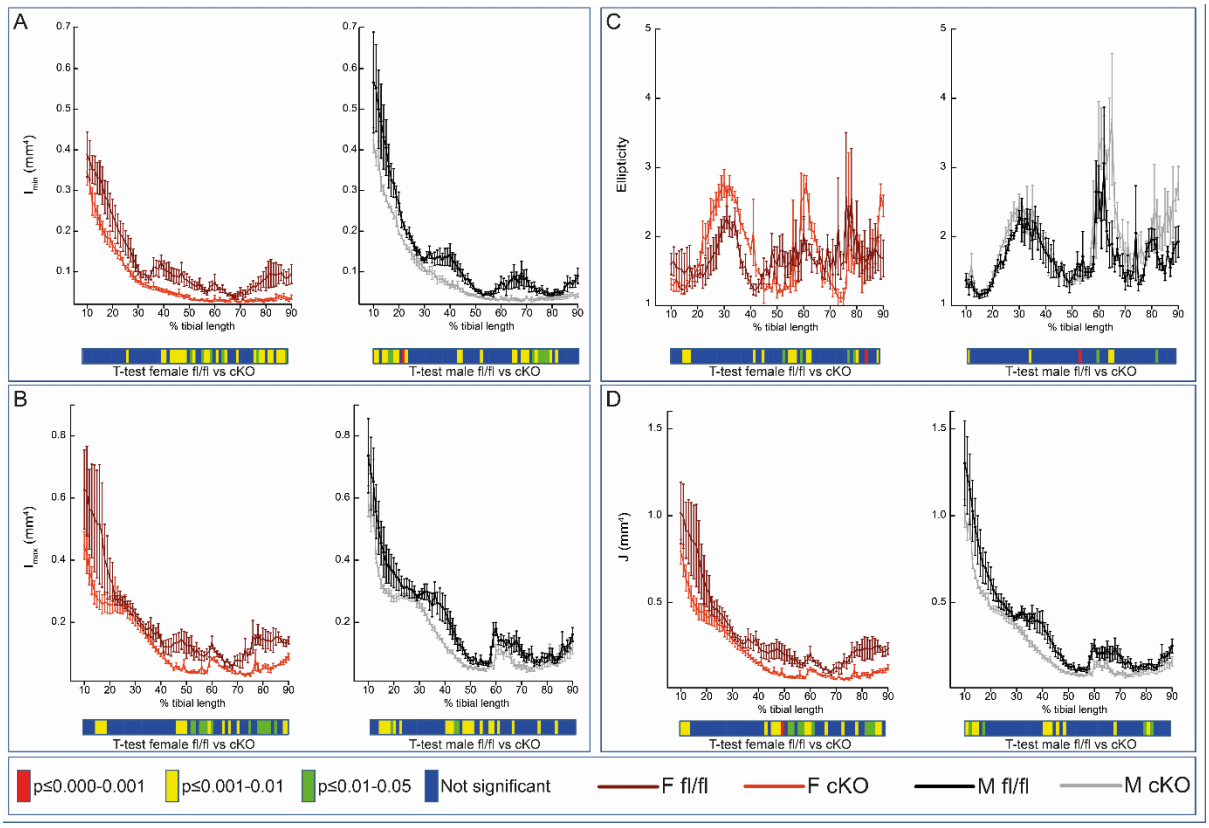
A
B
C
D
% tibial length
T-test female fl/fl vs cKO
T-test male fl/fl vs cKO
Ellipticity
J (mm⁴)
p≤0.000-0.001
p≤0.001-0.01
p≤0.01-0.05
Not significant
F fl/fl
F cKO
M fl/fl
M cKO

Figure 3

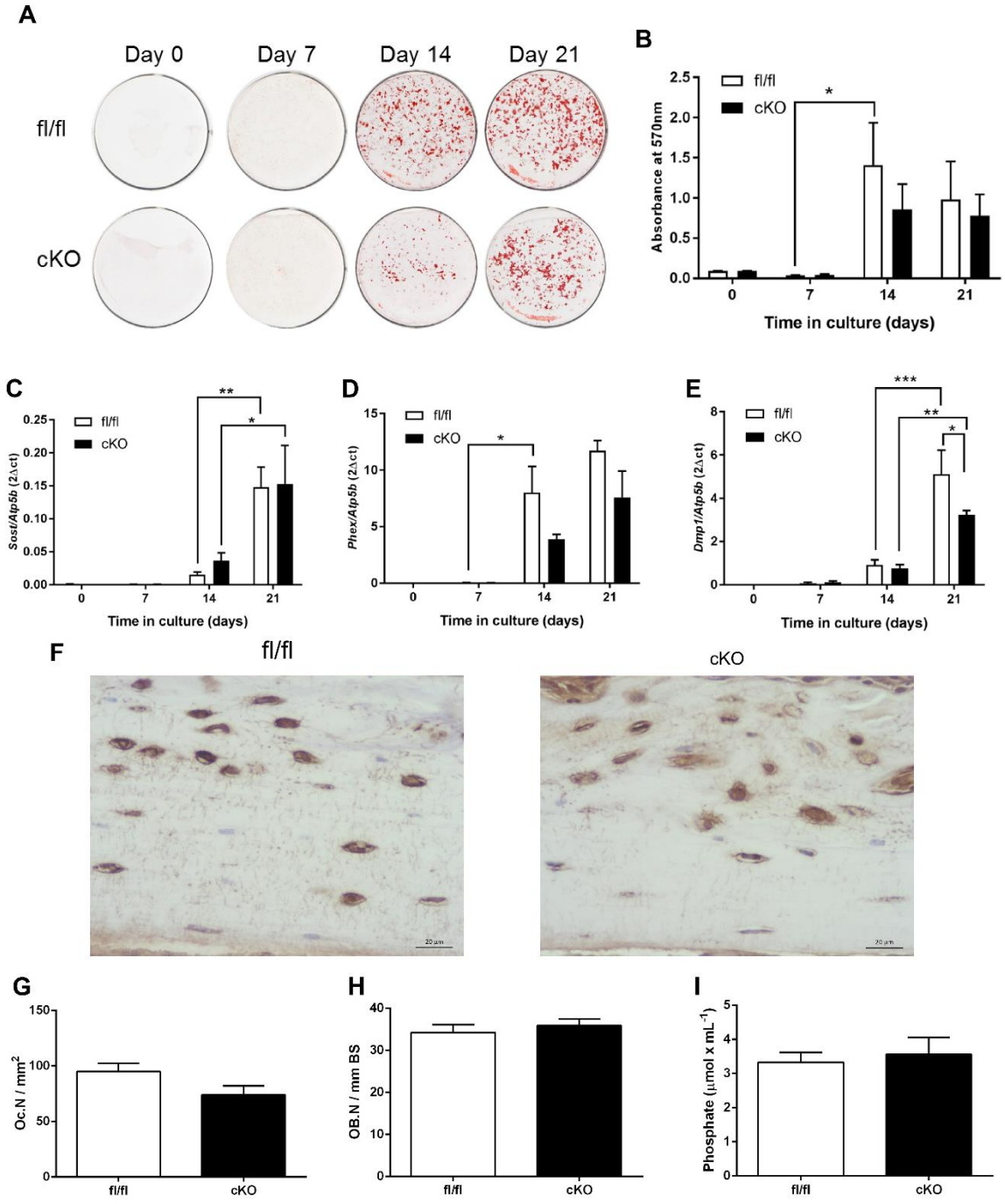
A
Day 0
Day 7
Day 14
Day 21
fl/fl
cKO
B
fl/fl
cKO
Absorbance at 570nm
Time in culture (days)
C
Sost/Atp5b (2Δct)
Time in culture (days)
D
Phex/Atp5b (2Δct)
Time in culture (days)
E
Dmp1/Atp5b (2Δct)
Time in culture (days)
F
fl/fl
cKO
G
Oc.N / mm2
H
OB.N / mm BS
I
Phosphate (μmol x mL-1)

Figure 4

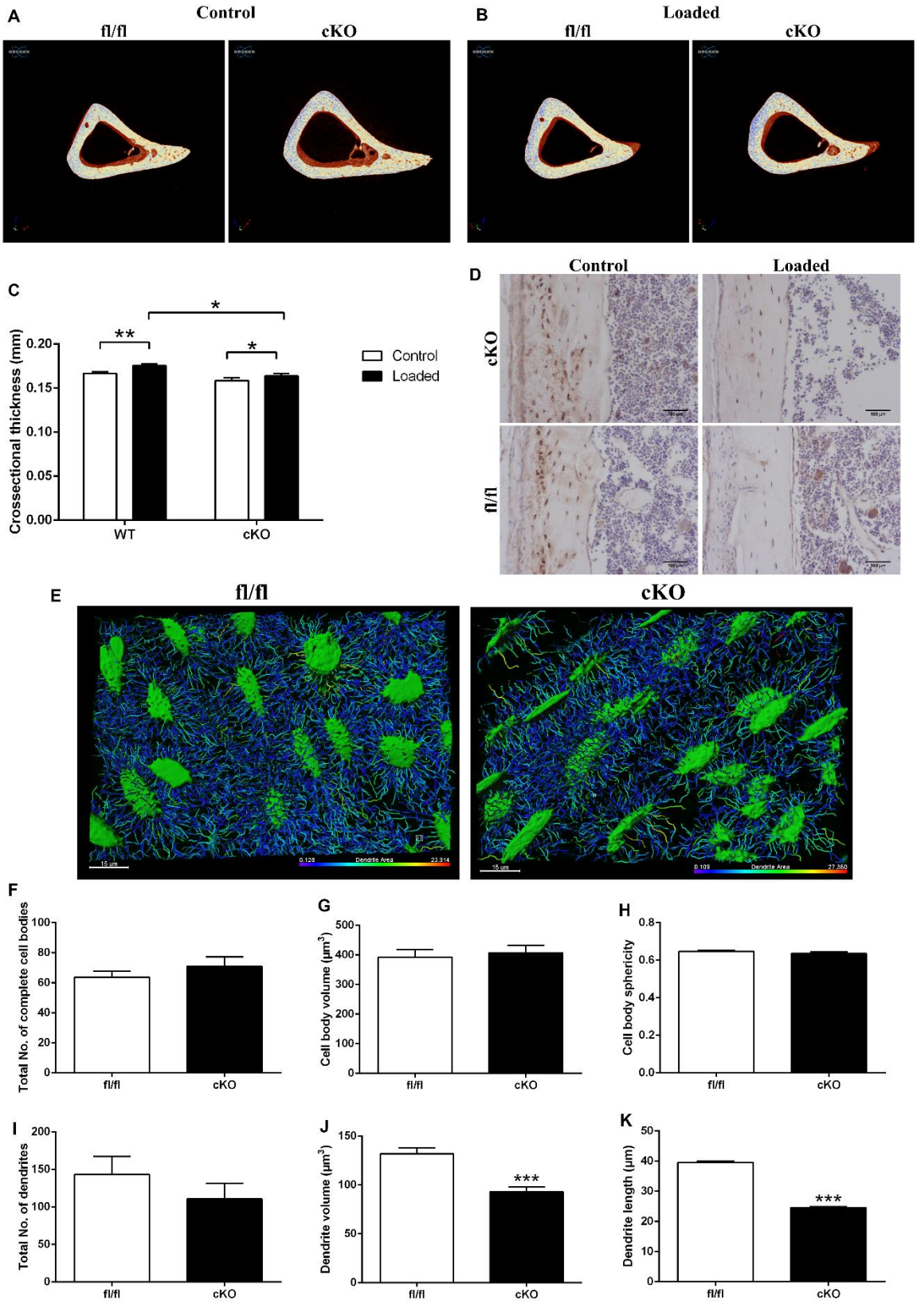
A
Control
fl/fl
cKO
B
Loaded
fl/fl
cKO
C
Crossectional thickness (mm)
0.20
0.15
0.10
0.05
0.00
**
*
*
Control
Loaded
WT
cKO
D
Control
Loaded
cKO
fl/fl
E
fl/fl
cKO
15 µm
Dendrite Area
F
Total No. of complete cell bodies
fl/fl
cKO
G
Cell body volume (µm³)
fl/fl
cKO
H
Cell body sphericity
fl/fl
cKO
I
Total No. of dendrites
fl/fl
cKO
J
Dendrite volume (µm³)
***
fl/fl
cKO
K
Dendrite length (µm)
***
fl/fl
cKO

Figure 5

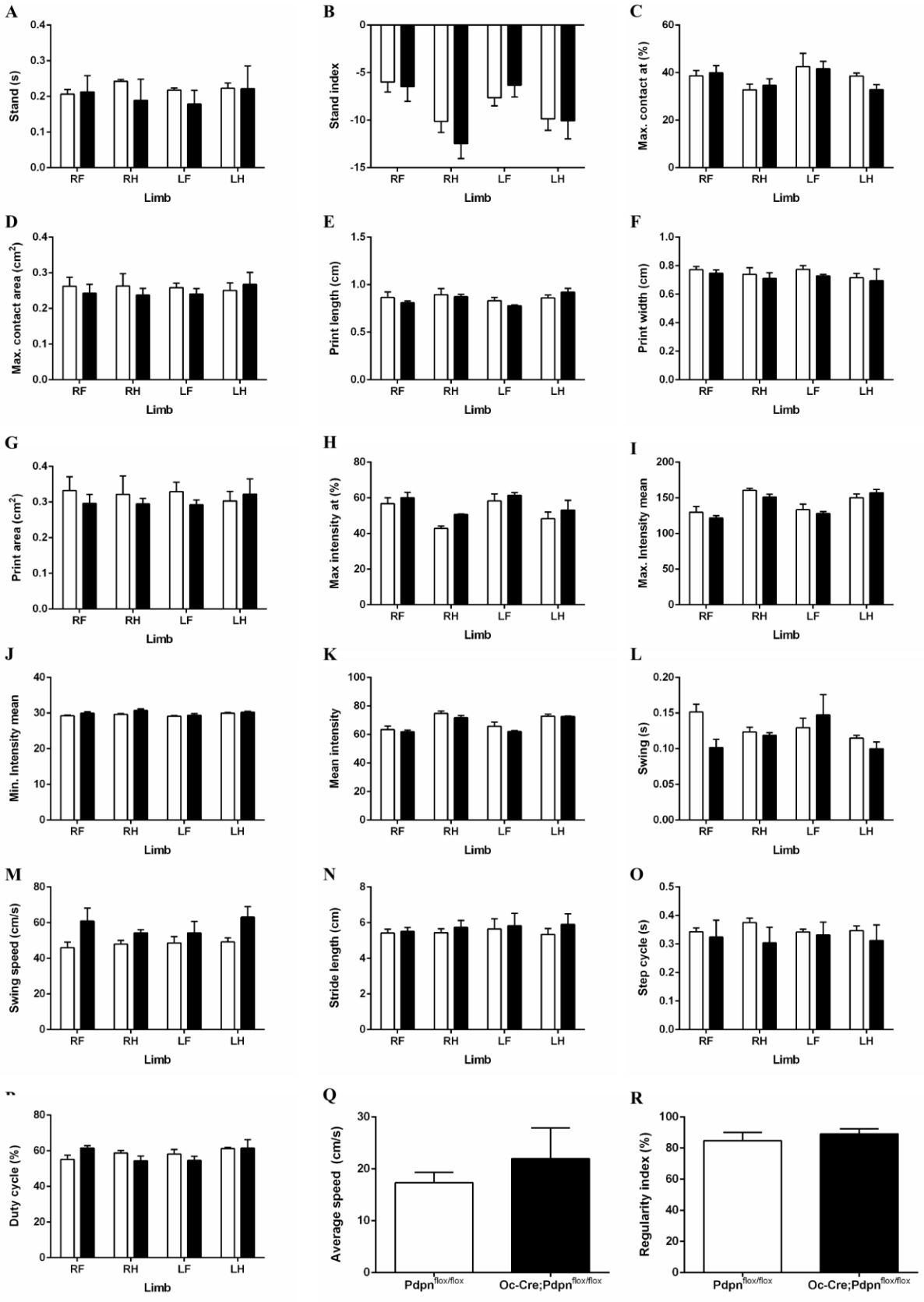
A
Stand (s)
0.4
0.3
0.2
0.1
0.0
RF RH LF LH
Limb
B
Stand index
0
-5
-10
-15
RF RH LF LH
Limb
C
Max. contact at (%)
60
40
20
0
RF RH LF LH
Limb
D
Max. contact area (cm²)
0.4
0.3
0.2
0.1
0.0
RF RH LF LH
Limb
E
Print length (cm)
1.5
1.0
0.5
0.0
RF RH LF LH
Limb
F
Print width (cm)
1.0
0.8
0.6
0.4
0.2
0.0
RF RH LF LH
Limb
G
Print area (cm²)
0.4
0.3
0.2
0.1
0.0
RF RH LF LH
Limb
H
Max intensity at (%)
80
60
40
20
0
RF RH LF LH
Limb
I
Max. Intensity mean
200
150
100
50
0
RF RH LF LH
Limb
J
Min. Intensity mean
40
30
20
10
0
RF RH LF LH
Limb
K
Mean intensity
100
80
60
40
20
0
RF RH LF LH
Limb
L
Swing (s)
0.20
0.15
0.10
0.05
0.00
RF RH LF LH
Limb
M
Swing speed (cm/s)
80
60
40
20
0
RF RH LF LH
Limb
N
Stride length (cm)
8
6
4
2
0
RF RH LF LH
Limb
O
Step cycle (s)
0.5
0.4
0.3
0.2
0.1
0.0
RF RH LF LH
Limb
Duty cycle (%)
80
60
40
20
0
RF RH LF LH
Limb
Q
Average speed (cm/s)
30
20
10
0
Pdpn flox/flox
Oc-Cre;Pdpn flox/flox
R
Regularity index (%)
100
80
60
40
20
0
Pdpn flox/flox
Oc-Cre;Pdpn flox/flox

Suppl Fig 1

Table 1: Trabecular parameters from microCT analysis of 6-week old male and female fl/fl, and cKO mice (n=4/genotype/sex). [a] P<0.05* in comparison to male equivalent genotype. Data are represented as mean ± S.E.M.

Sex		BV/TV (%)	Tb.N (μm^{-1})	Tb.Th (μm)	Tb.Sp (μm)	Tb.Pf (μm^{-1})
M	fl/fl	0.40 ± 0.05	1.14 ± 0.06	28.1 ± 3.53	1.19 ± 0.06	9.84 ± 3.71
	cKO	0.38 ± 0.03	1.12 ± 0.07	30.3 ± 1.57	1.11 ± 0.09	10.6 ± 3.12
F	fl/fl	0.23 ± 0.03[a]	1.19 ± 0.02	32.7 ± 1.65	0.96 ± 0.08	5.96 ± 3.05
	cKO	0.23 ± 0.03	1.07 ± 0.03	33.2 ± 3.36	1.12 ± 0.08	9.54 ± 2.68

Table 2: 3 point bending analysis of 6-week old male and female fl/fl, and cKO mice (n=4/genotype/sex). Data are represented as mean ± S.E.M. [a] P<0.05* in comparison to male equivalent genotype. [b] P<0.01** in comparison to female fl/fl. Data are represented as mean ± S.E.M.

Sex		Maximum load (N)	Deflection at Maximum Load (mm)	Work to Maximum Load (J)	Stiffness (N/m)	Load at Rupture (N)	Deflection at Rupture (mm)	Work to Rupture (J)
M	fl/fl	5.81 ± 0.65	0.60 ± 0.09	0.002 ± 0.00	17.7 ± 0.66	4.06 ± 0.45	0.80 ± 0.14	0.003 ± 0.00
	cKO	5.95 ± 0.26	0.78 ± 0.14	0.002 ± 0.00	16.4 ± 0.97	4.22 ± 0.19	1.08 ± 0.16	0.004 ± 0.00
F	fl/fl	4.58 ± 0.34	0.66 ± 0.04	0.002 ± 0.00	12.6 ± 1.42	3.21 ± 0.24[a]	0.90 ± 0.02	0.002 ± 0.00
	cKO	5.30 ± 0.51	0.68 ± 0.06	0.002 ± 0.00	19.1 ± 1.44[b]	3.88 ± 0.36	0.96 ± 0.11	0.003 ± 0.00

Table 3: Porosity parameters representing lacuna and vascular porosity of fl/fl and cKO mice detailing the effect of genotype. Data represent means ± SEM with group sizes of n = 4 for fl/fl and cKO mice.

Morphometric index	fl/fl n=4	cKO n=4	Effect of Genotype
Bone parameter			
Ct.TV (mm^{-3})	0.101 ± 0.017	0.078 ± 0.003	NS
Canal parameters			
N.Ca	52 ± 14.634	34 ± 12.124	NS
N.Ca/Ct.TV (mm^{-3})	530 ± 169.45	419 ± 134.24	NS
Ca.V/Ct.TV (%)	0.005 ± 0.001	0.003 ± 0.001	NS
Lacunae parameters			
N.Lc	1792 ± 353	1037 ± 383	NS
N.Lc/Ct.TV (mm^{-3})	18611 ± 4505	13083 ± 4497	NS
Lc.V/Ct.TV (%)	0.004 ± 0.000	0.003 ± 0.000	NS